Simulation-based Approach to Assessing Short-term Power Variations of PV Power Plants Under Cloud Conditions

Eric Bernard Dilger and Ricardo Vasques de Oliveira

***Abstract*—The output power variability of photovoltaic (PV) power plants (PVPPs) is one of the major challenges for the operation and control of power systems. The short-term power variations, mainly caused by cloud movements, affect voltage magnitude and frequency, which may degrade power quality and power system reliability. Comprehensive analyses of these power variations are crucial to formulate novel control approaches and assist power system operators in the operation and control of power systems. Thus, this paper proposes a simulation-based approach to assessing short-term power variations caused by clouds in PV power plants. A comprehensive assessment of the short-term power variations in a PV power plant operating under cloud conditions is another contribution of this paper. The performed analysis evaluates the individual impact of multiple weather condition parameters on the magnitude and ramp rate of the power variations. The simulation-based approach synthesizes the solar irradiance time series using three-dimensional fractal surfaces. The proposed assessment approach has shown that the PVPP nominal power, timescale, cloud coverage level, wind speed, period of the day, and shadow intensity level significantly affect the characteristics of the power variations.**

***Index Terms*—Photovoltaic (PV) generation, PV power plant, partial shading, cloud condition, power variation.**

I. Introduction

PHOTOVOLTAIC (PV) generation is a growing global trend that results in many challenges for modern power systems [1], [2]. The short-term power variations (or, equivalently, fast power variations) inherent to PV power plants (PVPPs) present a high level of unpredictability [3] and may require control intervention to ensure the grid code requirements established by system operators [1]. These fast power variations are mostly caused by cloud movements that attenuate the global solar irradiance on the ground [4]. Cloud coverage level, cloud opacity, and wind speed are the main weather condition parameters that directly affect short-term PVPP power variations [5].

Under typical weather conditions, ramp rates may exceed the limits specified by grid codes, posing a risk to power system stability and operational reliability [1], [6], [7]. Therefore, computational tools and other approaches to quantitatively accessing fast PVPP power variations are relevant for the operation and control of modern power systems [5], [8]-[10]. Proper computational tools and thorough assessments may provide a comprehensive understanding of the fast PVPP power variations and support operational decision-making and formulations of novel control approaches for PVPPs (or, equivalently, utility-scale PV systems) [5], [6], [11].

Different approaches can be employed to perform quantitative assessments of fast PVPP power variations, such as output power measurement-based approaches and simulation-based approaches. Simulation-based approaches may employ either measured solar irradiance or synthesized solar irradiance. The measurement and estimation of solar irradiance may be based on ground measurements and satellite images [4]. Power variation assessments using output power measurement-based approaches and solar irradiance measurement-based approaches usually neither characterize the weather condition parameters nor correlate such parameters with the power variation characteristics [12]-[16].

Satellite-based approaches are very useful for identifying cloud motion and spatial distribution, as well as forecasting changes under meteorological conditions on a timescale ranging from minutes to days. The satellite images can be converted to solar irradiance by cloud-to-irradiance algorithms [13]. However, cloud motion modeling based on satellite images is challenging, as stated in [6] and shown in [6], [16]. In addition, the spatial resolution of satellite images is typically in the order of a few kilometers, and the typical time resolution ranges from a few minutes to hours [4], [6], [13], [16]. Therefore, satellite-based approaches are not suitable and accurate enough to simultaneously generate multiple irradiance signals for the multiple PV units (PVUs) of a PVPP.

The output power variations in multiple PVPPs with different nominal power are assessed in [12], considering an

Manuscript received: May 3, 2024; revised: June 28, 2024; accepted: July 4, 2024. Date of CrossCheck: July 4, 2024. Date of online publication: August 26, 2024.

This work was supported in part by the Coordenação de Aperfeiçoamento de Pessoal de Nível Superior-Brasil (CAPES)-Finance Code 001. The authors acknowledge UTFPR-Campus Pato Branco, FINEP, SETI, CNPq, and Fundação Araucária for scholarships and funding.

E. B. Dilger is with Federal Institute of Paraná, Paraná, Brazil (e-mail: eric.dilger@ifpr.edu.br).

R. V. de Oliveira (corresponding author) is with the Electrical Engineering Department, Federal University of Technology, Paraná, 85503-390, Brazil (e-mail: vasques@utfpr.edu.br).

DOI: 10.35833/MPCE.2024.000460

output power measurement-based approach. Such assessment considers the power measurement over a period of one year with a one-second resolution and evaluates the magnitude of the power variations over different timescales. Other power variation assessments have also been performed considering output power measurement-based approaches [17]-[21]. However, the output power measurement-based approaches do not evaluate the individual impact of different weather condition parameters on the ramp rate and magnitude of the power variations, since they are based on measurements over a period with different weather condition parameters.

Simulation-based approaches that employ solar irradiance measurements require the adjustment of the spatial scale to determine the average solar irradiance incident on the surface of the PV arrays of interest, since the solar irradiances are typically measured by sensors at specific points [22]-[24]. Such spatial adjustment requires approaches based on functions that smooth the measured irradiance signal, such as moving average and transfer functions with low-pass filter characteristics [25]-[27]. However, the process employed to estimate the average irradiance over large geographical areas from irradiance measured by a sensor at a single point degrades the accuracy of the final average irradiance, since this process does not consider the spatial diversity of clouds and other relevant weather condition parameters. Despite being able to generate the average irradiance for equivalent PVPPs, irradiance signal generation approaches based on a single-point measurement are unable to generate simultaneously the irradiances for the multiple PVUs that compose a PVPP, since the spatial diversity of the clouds cannot be captured at a single point [28].

Wavelet-based variability models (WVMs) may correlate the irradiance between different sites. However, determining the correlation factor employed in WVMs requires dozens of irradiance sensors in large PVPPs [25], [26]. In addition, the correlation factor required by WVMs significantly varies over a timescale of hours to days, as a function of weather condition parameters. Therefore, the use of WVM in large PVPPs is restricted since it requires dozens of solar irradiance sensors and the continuous update of the correlation factor. In addition, the time-varying correlation factor is valid only for the geographical area from where the dozens of solar irradiance signals have been measured [25], [26].

Different from the other approaches, simulation-based approaches using synthesized cloud patterns allow the parameterization of the weather conditions. This remarkable advantage enables comprehensive assessments that consider the individual impact of each relevant weather condition parameter on all the PVUs of the PVPP. The cloud synthesis based on the fractal geometry theory, introduced in [29] and improved in [30], can be employed to formulate simulation-based approaches to effectively performing operational and control analyses in PVPPs and PV distributed generation units. In such an approach, synthesized shading surfaces are employed to generate realistic solar maps and irradiance time series.

A quantitative assessment of power ramp rates in PVPPs based on two-stage power conversion PVUs is performed in [28], also using a fractal-based approach. The approach presented in [28] considers a module-level irradiance synthesis, i.e., it generates the solar irradiance for each PV module of the PV system, and the PV array model for non-uniform irradiance [31]. Despite the increase in the emulation accuracy, the approach proposed in [28] is not suitable for large PVPPs based on multiple single-stage PVUs (or, equivalently, central inverter PVUs), since the computational expense increases considerably with the number of PV modules [32]. In addition, the fractal approach employed in [28] does not generate realistic elongated solar maps required to perform long-term simulations, since there is a discontinuity between the multiple frames of solar maps.

This paper formulates an approach to synthesizing solar maps and solar irradiance time series for fast power variation assessments and other planning, operation, and control studies of large PVPPs operating in cloudy weather. Fractal surfaces, derived from the concept of fractional Brownian motion, are used to generate the shading surfaces and the solar irradiances for all PVUs of the PVPP. As an innovative contribution, the methodology proposed in this paper considers the average value of the solar irradiance over the PV array of each PVU of the PVPP, since the resulting average irradiance presents an accurate linear relationship with the PVU output power [33]. In addition, the PVU PV array is represented by a typical equivalent PV module model [34]. The synthesized solar irradiance time series can be employed to perform multiple kinds of simulation-based analyses in large PVPPs considering predefined weather condition parameters. The main innovative contributions of this paper comprise:

1) Formulation of a solar irradiance synthesis approach capable of providing long-term simulations for PVPPs in the order of hundreds of megawatt: different from satellite and irradiance measurement-based approaches, the proposed fractal approach can simultaneously generate the solar irradiance time series for all PVUs that compose the PVPP, considering the spatial diversity of the clouds.

2) Comprehensive assessment of the fast PVPP power variations in a 100 MW PVPP operating under different cloud conditions: different from other simulation-based analyses, the impact of the PVPP nominal power, timescale, cloud coverage level, wind speed, period of the day, and shadow intensity level on the ramp rates and magnitudes of the power variations is comprehensively assessed.

The proposed methodology and performed analysis are helpful in supporting planning, operation, and control activities, such as voltage fluctuation analyses, frequency variation analyses, sizing of auxiliary devices (i.e., battery banks and dump loads), transmission line reinforcement, proposition of new requirements for grid codes, and formulation and assessment of novel control approaches. The typical control approaches related to PVPPs comprise power ramp control, power reserve control (or, equivalently, de-loaded control), inertia control, frequency control, and voltage control.

The remainder of paper is structured as follows. Section II addresses the fractal-based cloud shadow synthesis. The synthesis of solar maps and irradiance time series is presented in Section III. Section IV presents the assessment of power variations in a PVPP operating under cloud conditions. The conclusions are addressed in Section V.

II. Fractal-based Cloud Shadow Synthesis

The approach proposed in [29] and improved in [30] is employed to generate stochastic shadow patterns inherent to clouds. The solar maps are generated from the final shading surface based on predefined weather condition parameters that describe typical real cloud conditions. The cloud coverage level, wind speed, shadow intensity level, PV array coverage area, period of the day, period of analysis (or, equivalently, simulation period), and spatial resolution of the shading surface are conditions and parameters to provide a comprehensive assessment of the impact of cloud conditions on the operation of PVPPs.

The process of shadow emulation is divided into two stages, as addressed in the following subsections. The initial stage consists of synthesizing a three-dimensional fractal surface using the principles of fractional Brownian motion [29]. Subsequently, shading surfaces are synthesized by intersecting the fractal surface with several horizontal planes positioned at varying heights. The solar irradiance time series (i. e., irradiance signals) employed in time-domain simulations are generated based on the solar map (or, equivalently, final shading surface). Each elementary fraction of a given geographical area is represented by a pixel in such approach. The irradiance over a given geographical area can be generated considering a spatial resolution ranging from square centimeters to square meters.

A. Synthesis of Three-dimensional Fractal Surface

The classical midpoint displacement algorithm proposed in [29] to generate three-dimensional fractal surfaces is capable of generating only a single-square frame composed of $(N+1)\times(N+1)$ pixels. However, long simulation periods require a rectangular three-dimensional fractal (or, equivalently, elongated frame). The elongated fractal surface can be achieved by synthesizing multiple frames, as addressed in [30]. The longitudinal length of the shading surface is given by $F\times(N+1)$, where F is the number of frames employed to generate the fractal surface.

The employed midpoint displacement algorithm applies perpendicular displacement h to the central points of the squares and midpoints of the edges of the squares. Figure 1 illustrates the Cartesian plane corresponding to a single-square frame, defined by 25 points, where each point represents a pixel. The Cartesian plane is defined before the algorithm initialization as a matrix with the desired number of pixels $(N+1)\times(N+1)$. Thus, the algorithm calculates only the perpendicular displacement for each pixel (or, equivalently, the height h of each point in the third dimension, which is perpendicular to the Cartesian plane). In Fig. 1, the circles represent the known values of perpendicular displacement determined by the algorithm, while the diamonds represent the height h of each point to be determined in the current stage of the algorithm.

The recursive algorithm requires $M=\log_2 N$ stages to complete the surface calculation [30]. The fractal roughness is defined by the fractal dimension D. The assessment presented in [29] provides a suitable range of values for D to represent the shadows generated by clouds, suggesting the use of $D=1.9$ in the first half of the calculation process and $D=1.33$ in the remaining calculation process.

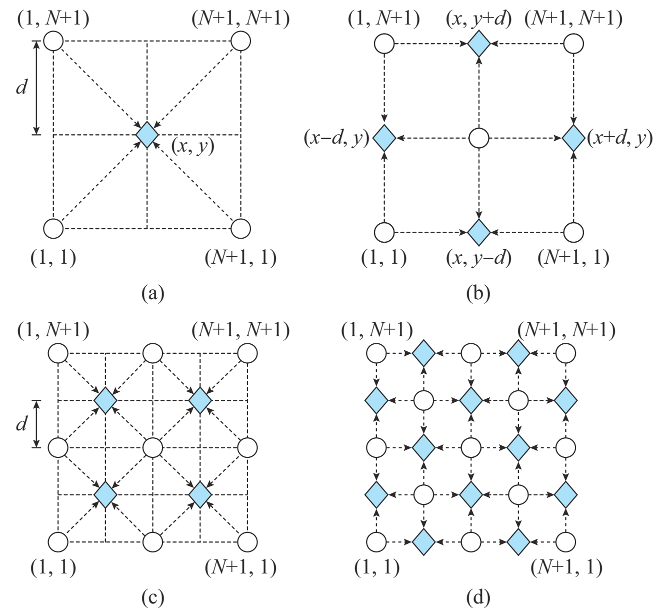

Fig. 1. Recursive process of two-dimensional midpoint displacement algorithm for $N=4$. (a) First stage for center midpoints. (b) First stage for edge midpoints. (c) Second stage for center midpoints. (d) Second stage for edge midpoints.

The values of the perpendicular displacement h of all pixels generated by the algorithm are stored in an $(N+1)\times(N+1)$ matrix $\boldsymbol{X}_{frac}$, which contains all the necessary points to represent a single frame of the three-dimensional fractal. In the cases of multiple frames used to generate an elongated fractal surface, $\boldsymbol{X}_{frac}$ has a dimension $(N+1)\times((N+1)\times F)$, where F is the number of employed frames. The discontinuity between multiple frames is eliminated by the modified algorithm proposed in [30]. In such an algorithm, the displacement values for the first column of pixels in each new frame $\boldsymbol{X}_{frac,p+1}$ $(p=1, 2, \ldots, F)$ are equal to the displacement values calculated for the last column of the previous frame $\boldsymbol{X}_{frac,p}$.

B. Synthesis of Solar Map

The three-dimensional fractal surface generated by the algorithm described in the previous subsection is employed to generate the final shading surface, which corresponds to a horizontal plane (i. e., two-dimensional fractal surface) characterized by the cloud coverage level and cloud opacity level. The cloud coverage level defines the proportion of the solar map that is shaded by clouds.

The shadow synthesis process, considering a single-fractal frame of 513×513 pixels, is illustrated in Fig. 2. The shading patterns are synthesized by intersecting the three-dimensional fractal with several horizontal layers at various levels (or, equivalently, horizontal planes), as illustrated in Fig. 2(a). The height h_{cut} of the main intersection layer is determined based on the desired cloud coverage level (or, equivalently, shadow level). The main intersection layer (or, equivalently, main cutting plane) generates a shading matrix $\boldsymbol{S}_{cut}$ composed of binary numbers representing the cloud shadow pattern shown in Fig. 2(b). Each position in the Cartesian plane of the fractal surface (or, equivalently, each pixel of $\boldsymbol{X}_{frac}$) corresponds to a unique point in the three-dimensional space that can be either above or below the given horizontal plane at height h_{cut} (main intersection layer). The value 1 is assigned to pixels of the shading matrix $\boldsymbol{S}_{cut}$ when the respective points of the fractal surface are below the intersection layer. The pixels of the shading matrix $\boldsymbol{S}_{cut}$ are assigned with the value 0 when the respective points of the fractal surface are above the intersection layer. The pixels with the value 1 form the shaded area. The higher the height of the horizontal plane, the greater the percentage of pixels with unit values in the shading matrix and, consequently, the higher cloud coverage level N_c.

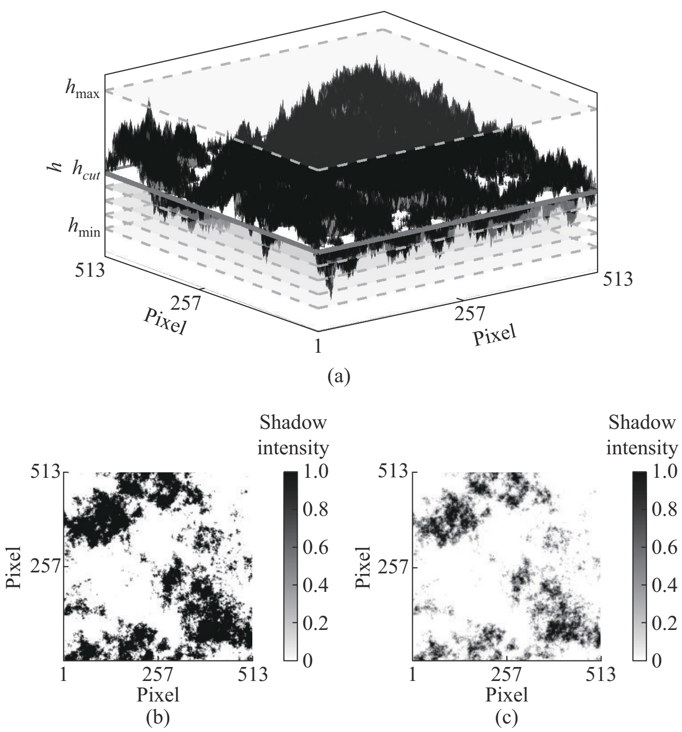

Fig. 2. Synthesis of shading surfaces from fractal surface. (a) Intersections between horizontal planes and fractal surface. (b) Shading surface generated by main intersection layer. (c) Final shading surface.

The irregular cloud thickness affects the shadow intensity. The clouds usually have higher opacity in their central part and lower opacity in their edges. This variable opacity is accounted for in the algorithm by using multiple additional intersection layers below the main intersection layer. These additional layers are placed at different heights of the h-axis, ranging from h_{cut} to $h_{\min}$, as depicted in Fig. 2(a). Each intersection layer results in a different shading matrix $\boldsymbol{S}_{cut,l}$. The final shading matrix $\boldsymbol{S}_f$, whose pixels range from 0 to 1, is determined by the average of all shading matrices (i. e., $\boldsymbol{S}_f = \dfrac{1}{q}\sum_{l=1}^{q}\boldsymbol{S}_{cut,l}$, where q is the number of intersection layers employed to generate the final shading matrix). The value of each pixel of the final shading matrix represents the shadow intensity I_s, which enables the generation of a rendered image to represent the final shading surface, as shown in Fig. 2(c).

III. Synthesis of Solar Maps and Irradiance Time Series

The maximum available power (MAP) of PVUs depends linearly on the global horizontal irradiance G_g, which is composed of a direct component G_{dir} and a diffuse component G_{dif}. The direct component, which is the dominant component of G_g, depends on cloud conditions and the angle between the sunlight and the ground surface [35]. The diffuse component corresponds to the sunlight portion scattered in the atmosphere. The diffuse component does not vary significantly with the cloud movement and thus can be assumed as constant [30]. The synthesis of the stochastic global irradiance over the PV array requires the direct and diffuse components of the irradiance as input.

The solar map is obtained using the transparency matrix $\boldsymbol{T}_f$, which quantifies the transparency intensity of the pixels I_t on a scale from 0 to 1. $\boldsymbol{T}_f$ is generated by subtracting an all-one matrix $\boldsymbol{S}_{ones}$ from the final shading matrix (i.e., $\boldsymbol{T}_f = \boldsymbol{S}_{ones} - \boldsymbol{S}_f$). A transparency intensity $I_t = 0.4$, for example, means that 40% of the direct irradiance passes through the cloud and reaches the area represented by one pixel or a set of pixels on the ground. A transparency intensity of 40% ($I_t = 0.4$) corresponds to a shadow intensity of 60% (i.e., $I_s = 1 - I_t = 0.6$, which means that the clouds attenuate 60% of the direct irradiance).

The global irradiance for each pixel on the solar map is determined by multiplying the direct irradiance by the transparency intensity of the pixel and then adding the resulting value to the considered diffuse irradiance (i. e., $G_g = I_t G_{dir} + G_{dif}$). Therefore, the solar map, the transparency matrix, and the shading matrix have the same dimension, as illustrated in Fig. 3. The impact of cloud conditions on PVPP operation can be assessed using the average global irradiance G_{gm} incident on the PV array of each PVU within the PVPP, since the PVU output power has a strong linear relationship with the average irradiance [33]. The average value of the transparency index I_{tm} of all pixels within the PV array area A_p is employed to calculate the global solar irradiance time series G_{gm}. The area A_p illustrated in Fig. 3 is represented by a portion of the transparency matrix $\boldsymbol{T}_{f,Ap}$. The transparency index of each pixel of $\boldsymbol{T}_{f,Ap}$ is employed to obtain the average transparency I_{tm} in area A_p. The proposed algorithm shifts the area A_p in the contrary direction of the wind speed to emulate the shadow movement over the PV array and synthesize the solar irradiance time series (or, equivalently, shifts the area A_p from the left to right side of the shading surface, as presented in Fig. 3(b)) where $\Delta d = v_w \Delta t$, where $\Delta t = t_k - t_{k-1}$ is the time resolution of the solar irradiance time series. Such relative motion is implemented in the algorithm by scanning the columns of $\boldsymbol{T}_f$ from left to right.

The set of pixels in $\boldsymbol{T}_f$, employed to synthesize the average solar irradiance incident in area A_p, is determined in the proposed algorithm based on the resolution of each pixel r_{pixel} (m^2), shadow speed v_w (m/s), simulation period t (s), and initial position of the area A_p. The average transparency intensity in each algorithm iteration $I_{tm}(t_k)$ is obtained by summing all the pixels within the area A_p in $\boldsymbol{T}_f$, weighted by the total number of pixels in area $A_p(N_p)$, as described in (1), where t_k is the sampling instant in the k^{th} sample. The solar irradiance time series can be generated considering a time resolution ranging from milliseconds to seconds.

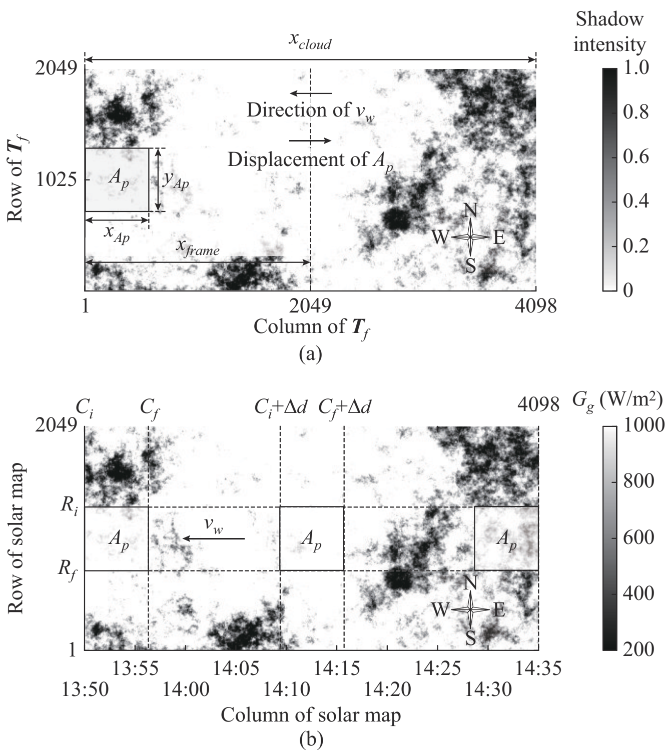

Fig. 3. Irradiance synthesis process. (a) Elongated transparency matrix $\boldsymbol{T}_f$. (b) Solar map with global irradiance generated from $\boldsymbol{T}_f$.

$$I_{tm}(t_k) = \frac{1}{N_p} \sum_{i=R_i}^{R_f} \sum_{j=C_i+v_w\Delta t}^{C_f+v_w\Delta t} T_{f,ij} \tag{1}$$

where $T_{f,ij}$ are the entries of the matrix $\boldsymbol{T}_f$.

The area A_p is characterized in (1) by the rows and columns of the matrix $\boldsymbol{T}_f$ that define the boundaries of the area A_p. These boundaries correspond to the initial row R_i, final row R_f, initial column C_i, and final column C_f, as illustrated in Fig. 3(b). The value of $I_{tm}(t_k)$ in each iteration is multiplied by the direct irradiance and summed with the diffuse component to calculate the average global irradiance $G_{gm}(t_k)$ over the area A_p, as described in (2). The direct irradiance can be obtained from a typical daily solar irradiance profile measured under clear sky conditions, such as the one presented in [36]. The diffuse irradiance may be considered constant, as addressed in the analysis performed in [30].

$$G_{gm}(t_k) = I_{tm}(t_k)G_{dir}(t_k) + G_{dif} \tag{2}$$

IV. Assessment of Power Variations in a PVPP Operating Under Cloud Conditions

The impact of cloud conditions on the fast PVPP power variations is comprehensively evaluated by time-domain simulations conducted using the Simulink toolbox of the MATLAB® software. The non-linear simulations have been performed using the ODE23s solver. A 100 MW PVPP composed of 25 PVUs with rated power of 4 MW is used as a test system, as shown in Fig. 4 [37]. Twenty five PVUs operate with low-voltage (LV) in the maximum power point tracking (MPPT), which are connected by medium-voltage power transformers (T-LV/MV) to the medium-voltage (MV) network. A high-voltage power transformer (T-MV/HV) connects the entire PVPP to the high-voltage (HV) power grid [38], [39]. The i^{th} PV array operates with irradiance G_i and temperature T_i.

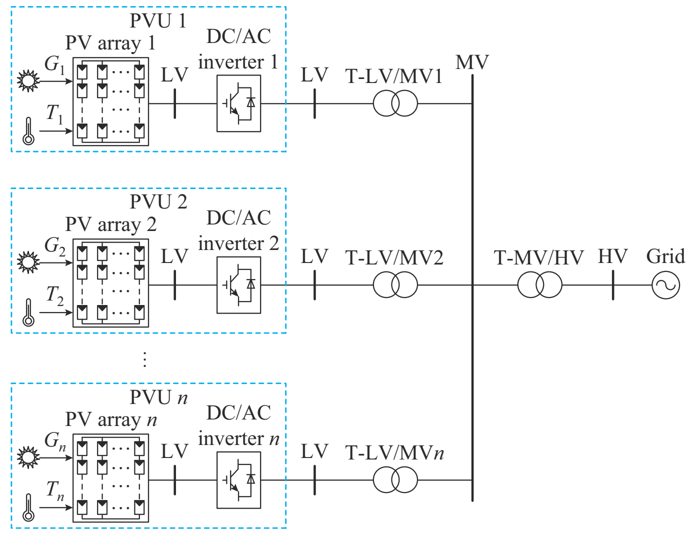

Fig. 4. Single-line diagram of employed PVPP.

The test PVPP is inspired by a real similar power plant evaluated in [32]. However, the proposed assessment approach is general enough to be applied to PV systems with nominal power ranging from a few kilowatt to a few gigawatt. The computational time required to generate the fractal and the irradiance signals for the 100 MW PVPP is 11 min using a typical laptop with an i7 processor and 16 GB of RAM, considering a time series of 6000 s.

PVUs correspond to single-stage PV systems, also known as central inverter PV systems [38]. The control loops of the PVUs regulate the generated reactive power and DC-link voltage at the DC bus between the PV array and inverter [39]. The classical perturb and observe (P&O) MPPT algorithm is employed to define the reference of the DC-link voltage, as illustrated in Fig. 5 [40].

The synchronous *dq* reference frame is employed in the inverter control system to provide a decoupled control of the reactive power Q and DC-link voltage V_{pv} [41]. A classical average model, considering the control loops and output filter and neglecting the pulse width modulation (PWM) and switching dynamics [42], is employed to represent the central inverter of the PVU. The inverter model is presented in [39], and the PV array model is presented in [41]. In Fig. 5, i_d and i_q are the output currents of the RL filter; v_d and v_q are the output voltages of the RL filter; v_a^*, v_b^*, and v_c^* are the voltage references of the inverter output; C_{dc} is the DC-link capacitance; r_f is the filter resistance; L_f is the filter inductance; I_{pv} is the output current of the PV array; θ is the phase angle of the grid voltage provided by the phase locked loop (PLL) to convert the voltages V_a, V_b, V_c and currents I_a, I_b, I_c to the dq reference frame; and Q_{meas} and Q_{ref} are the measured reactive power and reacticve power reference of the PVU, respectively.

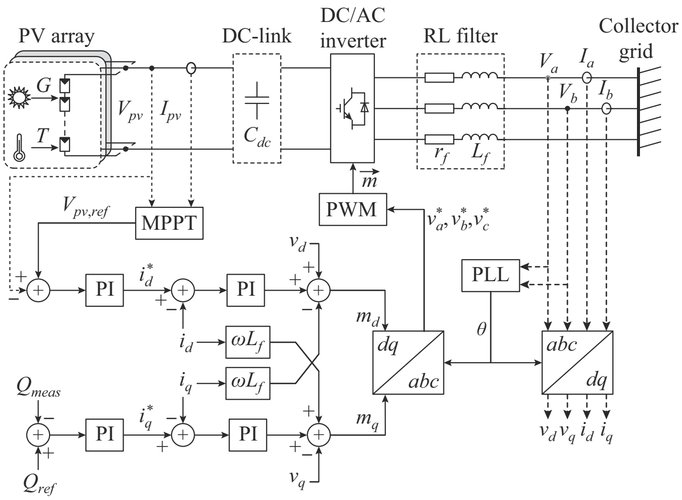

Fig. 5. General control diagram of employed PVU.

The DC-link voltage reference $V_{pv,ref}$ provided by the MPPT algorithm determines the maximum power point (MPP) of the PVU according to the solar irradiance and PV array temperature, as illustrated in the P-V curves of Fig. 6. The variables $V_{oc,i}$, $V_{MPP,i}$, and $P_{MPP,i}$ in Fig. 6 correspond to the open-circuit voltage, MPP voltage, and active power at the MPP, respectively.

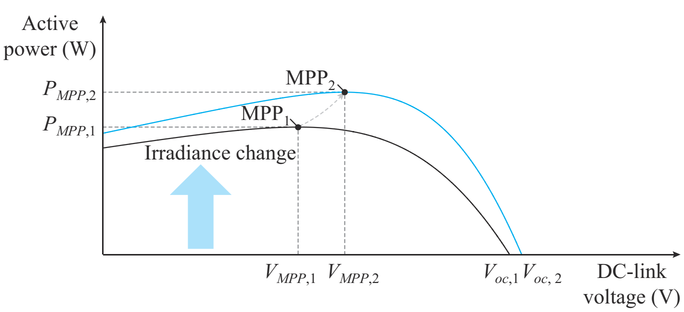

Fig. 6. The maximum power points on P-V curves for two different average global irradiances considering $G_{gm,2} > G_{gm,1}$.

The geographical location of 25 PVUs in the test PVPP is defined based on the layout of the the Quaid-e-Azam PVPP in Pakistan, with nominal power of 100 MWp [32]. The distribution of all PVUs in the shading surface is illustrated in Fig. 7. A resolution of 1 m^2 per pixel is considered to generate the shading surface composed of 12 million pixels.

The temporal series of the irradiance are generated using (1) and (2), considering a temporal resolution of 1 s ($\Delta t = 1$ s). A wind speed v_w of 7.5 m/s for the base case is selected based on the assessment presented in [27], [43]. The temporal series of the irradiance for the 25 PVUs are generated using the same three-dimensional fractal considering cloud coverage of 15%, 30%, and 60%, as shown in the solar map of Fig. 8.

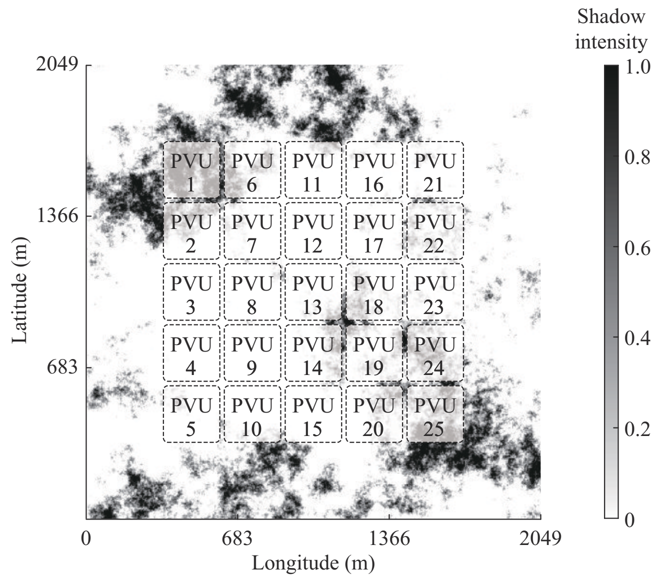

Fig. 7. Shading surface with geographical positions of PVUs.

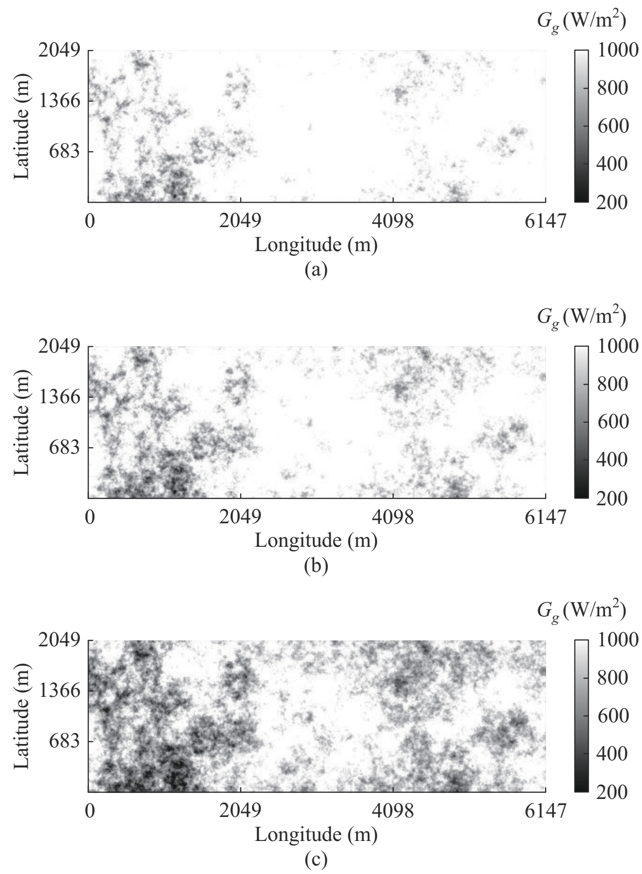

Fig. 8. Solar maps. (a) Cloud coverage level of 15%. (b) Cloud coverage level of 30%. (c) Cloud coverage level of 60%.

The PVPP rated power P_{nom}, timescale of power variations Δt_{ts}, cloud coverage level N_c, v_w, shadow intensity level I_{sm}, and period of the day (or, equivalently, G_{dir}) are the main aspects evaluated. The diffuse irradiance component is considered constant at 200 W/m^2 based on the analysis performed in [30], and the direct irradiance component is extracted from the daily solar irradiance profile presented in [36].

A solar irradiance time series with 6000 s is generated in the first stage of the assessment using the approach described in Section III. The algorithm to generate the irradiance has been implemented using programming code in the MATLAB® programming interface. In the sequence, the solar irradiance time series are exported to the Simulink toolbox of the MATLAB® and used as input signals for the 25 PVUs of the PVPP model.

The percentage variation of the PVPP output power $\Delta P_{\Delta t}(t_k)$ is a quantitative index used in the assessment. The power variation is calculated over a timescale of 20 s ($\Delta t_{ts}=$ 20 s) and normalized by P_{nom}, as defined in (3) [12].

$$\Delta P_{\Delta t}(t_k)=\frac{P(t_k)-P(t_k-\Delta t_{ts})}{P_{nom}}\times 100 \tag{3}$$

The ramp rate of the PVPP output power RR, defined in (4), is also employed as a quantitative index in the performed analysis [44]. The RR, in %/min, is calculated using a moving time window of 1 min ($\Delta t_{ts}=1$ min) and a resolution of 1 s ($t_{k-1}-t_k=1$ s), as employed in [44].

$$RR(t_k)=\frac{P(t_k)-P(t_k-\Delta t_{ts})}{P_{nom}\Delta t_{ts}}\times 100 \tag{4}$$

The following parameters are employed in the base case scenario: PVPP nominal power of 100 MW, timescale of 20 s for the power variation index, cloud coverage level of 60%, wind speed of 7.5 m/s, the maximum global solar irradiance of 1000 W/m^2 (operation in the midday hours), and average shadow intensity of 30%. The impact of each one of the parameters at a time is evaluated in the following subsections, keeping the remaining parameters constant. The absolute values of the power variation samples are considered to determine the mean and maximum values of the power variation magnitudes (ΔP_{mean} and $\Delta P_{\max}$). The mean and maximum absolute values of the power ramp rate (RR_{mean} and $RR_{\max}$) are also evaluated in the performed analysis.

A. Impact of PVPP Nominal Power on Ramp Rates and Magnitudes of Power Variations

The PVPP nominal power determines the geographical area occupied by the PV arrays, which affects the characteristics of the average irradiance variability in the entire PVPP. Three PVPPs with the rated power of 4 MW, 36 MW, and 100 MW are considered in such analysis. The time response of the PVPP output power in each scenario is illustrated in Fig. 9, and Table I provides the ramp rates and magnitudes of the power variations for the three scenarios.

It is possible to see that the power variation magnitudes increase with the PVPP nominal power. However, the mean and maximum values of the power variations given by (3) and (4) decrease with the increase in the PVPP nominal power. The 4 MW PVPP, for example, exhibits a maximum percentage of power variation, which is 5.79 times higher than that observed in the 100 MW PVPP. The increase in the nominal power has a smoothing effect on the power variations because the impact of new shadows arriving overlarge geographical areas is partially compensated by the shadows leaving such large areas. This compensation phenomenon is not significant in small geographical areas (or, equivalently, small PVPPs), since the typical size of the shadows caused by clouds may completely cover such small areas. In addition, the clear sky areas between the clouds may generate unshaded areas that can completely illuminate small PV arrays during a short time period, causing fast irradiance variations with large amplitude due to the fast transition between shaded and unshaded irradiances. According to the results, increasing the nominal power reduces the risk posed by power variations on power system reliability.

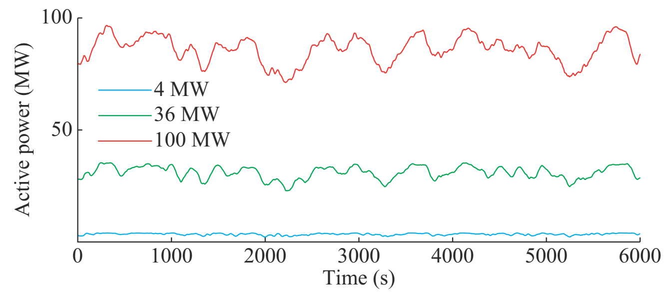

Fig. 9. Output power for three PVPPs with different rated power.

TABLE I
RAMP RATES AND MAGNITUDES OF OUTPUT POWER VARIATIONS FOR THREE PVPPS WITH DIFFERENT RATED POWER

P_{nom} (MW)	ΔP_{mean} (%)	$\Delta P_{\max}$ (%)	RR_{mean} (%/min)	$RR_{\max}$ (%/min)
4	4.65	21.27	8.82	34.76
36	1.93	7.30	5.01	15.35
100	1.11	3.67	2.80	9.74

The impact of the obtained quantitative results on the power system is relative, as it depends on the constructive and operational characteristics of each specific power system, such as the R/X ratio, equivalent inertia constant H_{eq}, and approaches employed to regulate the frequency and magnitude of the system voltage. A power ramp rate of 10%/min, for example, is defined as the maximum allowable value for PV systems in Germany and Puerto Rico, while the Denmark grid code defines 100 kW/s as the maximum allowable power ramp rate for PV systems higher than 11 kW [28]. A fast PVPP power variation in the order of dozens of MW could not induce a relevant fast voltage variation in a network with R/X ratio of 0.06, but it could result in a substantial fast voltage variation in a network with R/X ratio of 0.25. Therefore, the impact level of the fast power variations from a specific PVPP depends on additional studies, such as power flow and other analyses that require further information beyond the quantitative results presented in this paper. The fast PVPP power variation indexes serve as input data for other power system studies.

B. Impact of Timescale on Magnitudes of Power Variations

The timescale is an important aspect of power variations, since many grid-codes usually define ramp rate limits based on different timescales (i. e., maximum MW/min or maximum instantaneous MW/s). The voltage control system presents a timescale ranging from milliseconds to a few seconds, while the frequency control system presents a timescale ranging from seconds to a few minutes.

The performed analysis considers power variations in the typical timescales of the voltage and frequency control systems. The power variations are evaluated for the 100 MW PVPP considering the timescales of 5 s, 20 s, and 60 s (i.e., $\Delta t_{ts}=5$ s, $\Delta t_{ts}=20$ s, and $\Delta t_{ts}=60$ s, where Δt_{ts} is the moving time window employed in (3) and (4)). The other weather condition parameters correspond to the base case parameters. Figure 10 presents the probability density distributions of the magnitudes of power variation for different timescales, and Table II provides the ramp rates and magnitudes of the output power variations in different timescales for 100 MW PVPP. The statistical analysis is generated based on the output power presented in Fig. 9, with a period of 6000 s.

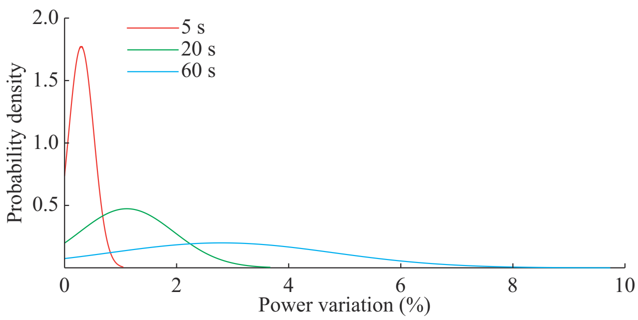

Fig. 10. Probability density distributions of magnitudes of power variation for different timescales.

TABLE II
RAMP RATES AND MAGNITUDES OF OUTPUT POWER VARIATIONS IN DIFFERENT TIMESCALES FOR 100 MW PVPP

Δt_{ts} (s)	ΔP_{mean} (%)	$\Delta P_{\max}$ (%)	RR_{mean} (%/min)	$RR_{\max}$ (%/min)
5	0.30	1.04	3.58	12.51
20	1.11	3.67	3.34	11.02
60	2.80	9.74	2.80	9.74

The probability density curve for the power variations in the timescale of 5 s indicates a higher probability for smaller magnitude variations compared with the other timescales. In the timescale of 60 s, the distribution curve widens, which corresponds to a decrease in the number of smaller-magnitude variations and an increase in the number of higher-magnitude variations. The timescale of 60 s results in a maximum power variation of 9.74%, which is 9.36 times greater than the maximum variation observed in the timescale of 5 s. Timescales higher than 20 s present power variations with significant magnitudes, which are consequently more prone to disturbing the voltage magnitude. The average and maximum ramp rates have increased with the decrease of the timescale due to the reduction of the moving time window Δt_{ts} in the denominator of (4).

C. Impact of Cloud Coverage Level on Ramp Rates and Magnitudes of Power Variations

N_c affects the ramp rate and the magnitude of the variations in the PVPP output power. Cloud coverage levels corresponding to 15%, 30%, and 60% are employed in the analysis and the other weather condition parameters corresponding to the base case parameters. It is worth remarking that cloud coverage levels higher than 60% typically occur in many regions of the planet [4].

Figure 11 presents the output power of the 100 MW PVPP for different cloud coverage levels. The results demonstrate that the average power generated significantly decreases as the cloud coverage level increases. However, the ramp rate and magnitude of the power variations significantly increase as the cloud coverage level increases.

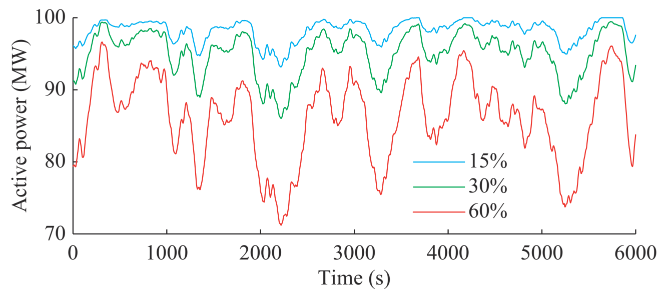

Fig. 11. Output power of 100 MW PVPP for different cloud coverage levels.

In Table III, the ramp rates and magnitudes of the output power variations is presented in the three employed scenarios, considering the base case timescales. The cloud coverage level increases from 15% to 60%, which also increases the mean and the maximum percentage of power variation by 3.82 and 2.02 times, respectively. These results indicate that the PVPP operation becomes more critical with the increase in cloud coverage. The mean and maximum power ramp rates also increase significantly as the cloud coverage level increases.

TABLE III
RAMP RATES AND MAGNITUDES OF OUTPUT POWER VARIATIONS FOR DIFFERENT CLOUD COVERAGE LEVELS

N_c (%)	ΔP_{mean} (%)	$\Delta P_{\max}$ (%)	RR_{mean} (%/min)	$RR_{\max}$ (%/min)
15	0.29	1.82	0.67	3.42
30	0.59	2.67	1.42	5.81
60	1.11	3.67	2.80	9.74

D. Impact of Wind Speed on Ramp Rates and Magnitudes of Power Variations

The wind speed determines the cloud speed (or, equivalently, shadow speed), which in turn affects the power variations. This analysis considers typical shadow speeds v_w obtained from real measurements in [27], [43]. Shadow speeds of 5.0 m/s, 7.5 m/s, and 10 m/s are employed in this analysis and the other weather condition parameters correspond to the base case parameters. It is worth remarking that shadow speeds higher than 10 m/s typically occur in many regions of the planet [27], [43].

The output power of the 100 MW PVPP for the different shadow speeds is shown in Fig. 12. The average values of the output power in the three scenarios are similar. However, the ramp rates and magnitudes of the output power variations increase with the increase of the shadow speed.

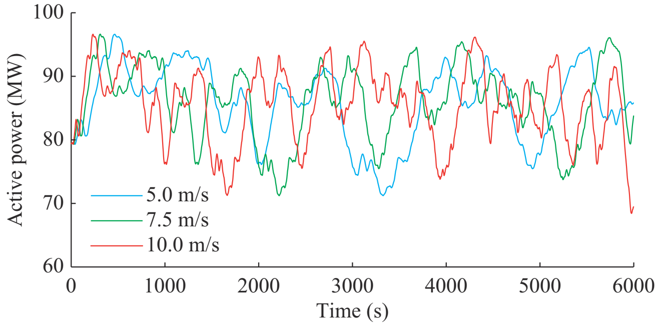

Fig. 12. Output power of 100 MW PVPP for different shadow speeds.

In Table IV, the quantitative indexes of the power variations observed in Fig. 12 are presented. The mean and maximum values of the ramp rates and magnitudes of the output power variations increase significantly with the increase of the shadow speed. Therefore, as the wind speed increases, the ramp rates and the magnitudes of the output power variations deteriorate. The analysis shows that cloudy days with high wind speed result in critical operational conditions for PVPPs.

TABLE IV
RAMP RATES AND MAGNITUDES OF OUTPUT POWER VARIATIONS FOR DIFFERENT SHADOW SPEEDS

v_w (m/s)	ΔP_{mean} (%)	$\Delta P_{\max}$ (%)	RR_{mean} (%/min)	$RR_{\max}$ (%/min)
5.0	0.78	2.61	2.06	6.73
7.5	1.11	3.67	2.80	9.74
10.0	1.50	5.02	3.76	11.80

E. Impact of Period of Day on Ramp Rates and Magnitudes of Output Power Variations

The period of the day determines the average direct solar irradiance and, consequently, affects the characteristics of the output power variations. The daily solar irradiance profile experimentally obtained in [36] is employed in the analysis. Three operational scenarios are employed considering three different periods of the day: ① morning period, from 07:00 to 08:40, when the global irradiance is the lowest (≈400 W/m^2); ② midday period, from 12:00 to 13:40, representing the period with the highest irradiance value (≈1000 W/m^2); ③ afternoon period, from 15:00 to 16:40, characterized by an intermediate value of global irradiance (≈710 W/m^2). The weather condition parameters corresponding to the base case are employed in this analysis. Figure 13 presents the output power of 100 MW PVPP for different periods of the day, and the quantitative indexes for the output power variations are presented in Table V.

In the early morning, the output power variations present smaller ramp rates and smaller magnitudes compared with the other periods. The end of the afternoon also presents a similar behavior. The output power variations present higher ramp rates and higher magnitudes at midday. The mean values of the magnitude and ramp rate of the output power variations at midday are 2.41 and 2.35 times higher than the mean values observed in the early morning, respectively, as presented in Table V. This analysis quantitatively shows that the midday period is the critical period for PVPPs operating under cloud conditions.

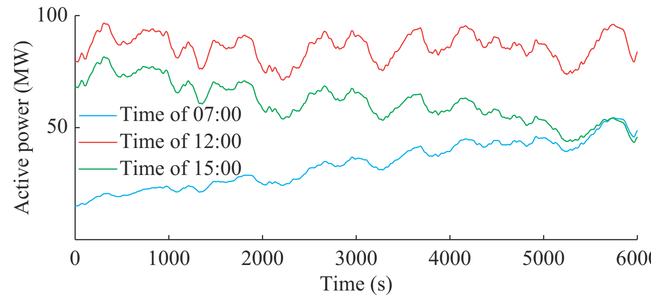

Fig. 13. Output power of 100 MW PVPP for different periods of day.

TABLE V
RAMP RATES AND MAGNITUDES OF OUTPUT POWER VARIATIONS FOR DIFFERENT PERIODS OF DAY

G_{gm} (W/m²)	ΔP_{mean} (%)	$\Delta P_{\max}$ (%)	RR_{mean} (%/min)	$RR_{\max}$ (%/min)
400	0.46	1.93	1.19	5.38
710	0.81	2.93	2.02	7.16
1000	1.11	3.67	2.80	9.74

F. Impact of Shadow Intensity Level on Ramp Rates and Magnitudes of Output Power Variations

Clouds with higher amount of water particles have higher opacity, and consequently, more intense shadows. Additionally, the central region of clouds is typically characterized by a higher opacity compared with the cloud edges. The opacity of clouds mainly attenuates the direct component of the solar irradiance, affecting the global irradiance in the PV arrays. The performed analysis evaluates the impact of the shadow intensity on output power variations for average shadow intensity levels I_{sm} of 20%, 30%, and 40%. A mean value of shadow intensity levels equal to 40% has been observed in the measurement-based assessment presented in [28]. A shadow intensity level of 40%, for example, means that 40% of the direct component of the solar irradiance is attenuated by the clouds. The other weather condition parameters corresponding to the base case are employed in this analysis.

The responses of the PVPP output power for the three employed scenarios are presented in Fig. 14.

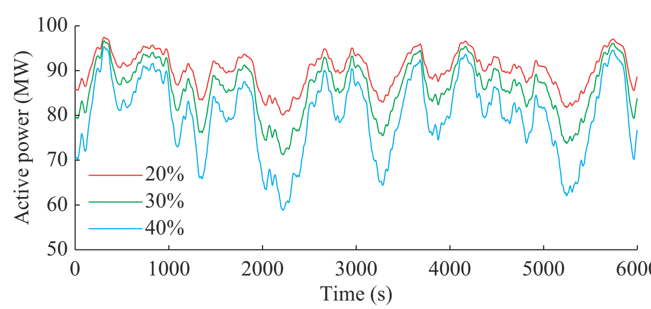

Fig. 14. Output power of 100 MW PVPP for different shadow intensity levels.

The results show that the increase in the shadow intensity increases the ramp rates and the magnitudes of the output power variations and decreases the minimum and average generated power. In the scenarios corresponding to shadow intensity level of 20% and 40%, the minimum values of the PVPP output power are 80.13 MW and 58.81 MW, respectively.

In Table VI, the quantitative indexes of the power variations shown in Fig. 14 are presented. The mean values of the ramp rates and magnitudes of the output power variations in the scenario with the shadow intensity level of 40% are 2.11 and 2.13 times higher than the mean values observed in the scenario with the shadow intensity level of 20%, respectively. The maximum values of the output power variation indexes have also increased significantly with the increase of the shadow intensity level. The analysis shows that the increase of the shadow intensity level deteriorates the ramp rates and magnitudes of the output power variations, as well as reduces the average generated power. Therefore, days with high relative humidity are more critical in terms of the risk that output power variations pose to the power system reliability.

TABLE VI
RAMP RATES AND MAGNITUDES OF OUTPUT POWER VARIATIONS FOR DIFFERENT SHADOW INTENSITY LEVELS

I_{sm} (%)	ΔP_{mean} (%)	$\Delta P_{\max}$ (%)	RR_{mean} (%/min)	$RR_{\max}$ (%/min)
20	0.76	2.48	1.91	6.61
30	1.11	3.67	2.80	9.74
40	1.61	5.24	4.07	14.07

G. Irradiance Measurement-based Approaches: A Comparative Analysis

Two different irradiance measurement-based approaches are employed to perform a comparison analysis. The low-pass filter-based approach [45] and the time averaging-based approach [25], [46] have been employed to generate the output power of the employed test system (i.e., 100 MW PVPP) considering the cloud coverage level of 60% presented in Section IV-C. These two approaches considered require a single-point irradiance measurement. The single-point irradiance signal is generated by a virtual solar irradiance measurement in the test PVPP. A single pixel of the PVPP footprint is used as a virtual sensor to generate the irradiance signal for the irradiance measurement-based approaches.

The low-pass filter-based approach is based on the transfer function (5).

$$\frac{P_{out}}{G_t} = \frac{P_{nom}/G_{nom}}{1+\sqrt[s]{A_{PVPP}}/2\pi f_c} \tag{5}$$

where A_{PVPP} is the area of the PVPP footprint; $f_c = 0.02A_{PVPP}^{-0.499}$ is the irradiance cut-off frequency; P_{out} is the output power of the PVPP; G_{nom} is the nominal irradiance; and G_t is the signal corresponding to the single-point irradiance measurement [45].

The length of the time window corresponding to the time averaging-based approach t_{avg} is given by (6).

$$t_{avg} = \frac{\sqrt{A_{PVPP}}}{v_w} \tag{6}$$

Two scenarios are evaluated in the proposed comparison analysis: ① virtual sensor placed at the center of the PVPP, which corresponds to the center of the PV array of PVU 13; ② virtual sensor placed at the upper corner of the PVPP, which corresponds to the center of the PV array of PVU 1. The output power of the 100 MW PVPP, generated by the different approaches in the two scenarios, is presented in Fig. 15. The single-point irradiance measurements corresponding to the two scenarios are presented in Fig. 16. The output power generated by the fractal-based approach is employed as a reference case, since the solar map generated by the fractal is used to generate the single-point irradiance signal used in the other two approaches. In addition, the reference case considers the cloud spatial diversity and other weather condition parameters.

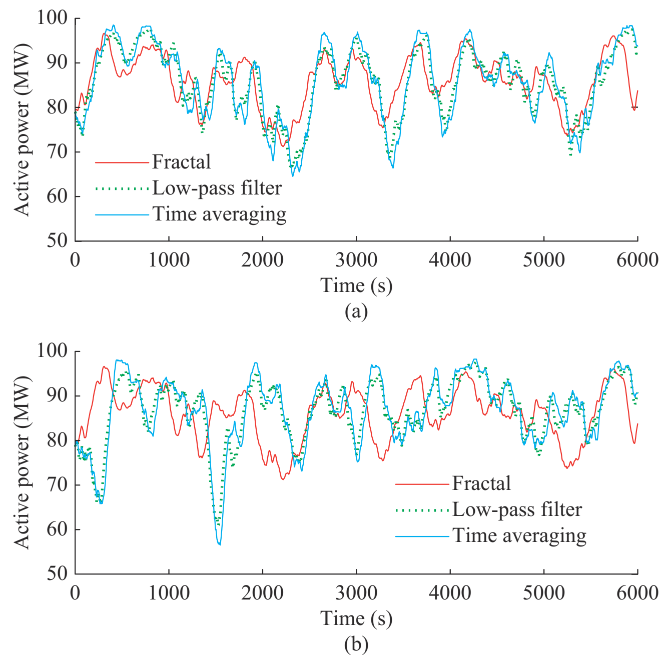

Fig. 15. Output power of test PVPP. (a) Output power of PVPP for irradiance measured at center of PVU 13. (b) Output power of PVPP for irradiance measured at center of PVU 1.

The results show that the measurement point significantly affects the equivalent output power generated by the irradiance measurement-based approaches. The output power in the two scenarios is significantly different because the irradiances measured at the two different points of the PVPP are significantly different, as shown in Fig. 16. It can be observed that the maximum and average relative errors are more significant in the scenario corresponding to the irradiance measured at PVU 1. Relative percentage errors of 31.24% for the low-pass filter-based approach and 35.84% for the time averaging-based approach are observed in the scenario corresponding to the measurement at PVU 1. Relative percentage errors of 19.88% and 20.96% for the low-pass filter-based and time averaging-based approaches, respectively, are observed in the scenario corresponding to the measurement at PVU 13.

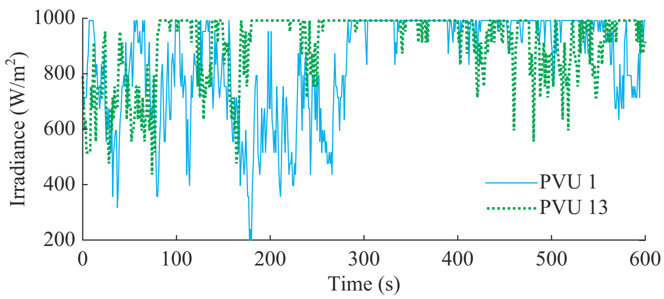

Fig. 16. Solar irradiance measured at two different points.

Different from the other approaches, the cloud spatial diversity inherent to the fractal-based approach allows the synthesis of the average solar irradiance for each PVU of the PVPP based on a realistic solar map. The output power of PVUs 1, 13, and 25, generated by the fractal-based approach, is shown in Fig. 17. The cloud spatial diversity results in a highly heterogeneous behavior for the three PVUs. At $t=185$ s, for example, the output power of PVU 25 is 1.59 times higher than that of PVU 1. The individual irradiance and output power at each PVU are essential for proposing and evaluating control approaches, since PVPPs are controlled at the PVU level. The output power of each PVU, for example, is required in voltage and de-loaded control approaches [37].

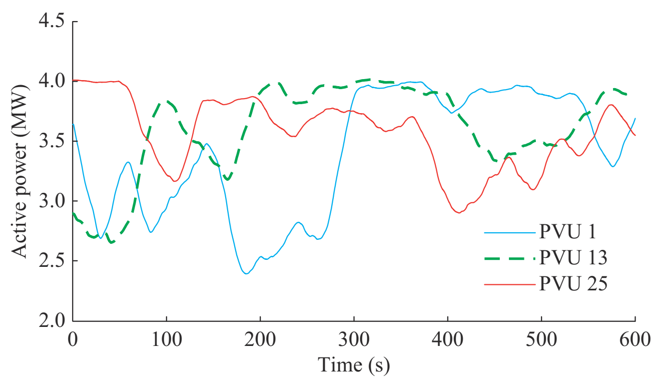

Fig. 17. Heterogeneous output power of PVUs 1, 13, and 25.

V. Conclusion

A methodology to generate solar maps and solar irradiance time series is proposed to assess fast power variations and support planning, operation, and control activities in large PVPPs under cloud conditions. The approach can simultaneously generate the irradiances for all the multiple PVUs within a given PVPP. Three-dimensional fractals are employed to synthesize the average irradiance, considering predefined weather condition parameters that describe typical real cloud conditions, such as cloud coverage level, wind speed, and shadow intensity level.

A comprehensive assessment of the stochastic power variations inherent to large PVPPs is conducted based on a long-term simulation considering a detailed dynamic model for all PVUs. The proposed approach is employed to provide the irradiance time series for the 25 PVUs of a 100 MW PVPP. The analyses demonstrate that the increase in the cloud coverage level, wind speed, and shadow intensity level significantly increases the ramp rates and magnitudes of the output power variations of the PVPP. Besides, the ramp rates and magnitudes of the power variations of the PVPP decrease with the increase in the rated power of the PVPP.

The proposed approach and the performed analysis consider the average irradiance over the entire PV array of each PVU. Therefore, they are not intended to assess non-uniform irradiance conditions on an individual module-level scale (i. e., solar irradiance for each PV module of the PV array).

The proposal of a dynamic simulation approach based on the integration of the irradiance synthesis approach, and a simplified model for large PVPPs with all their multiple PVUs is a future direction of this research.

References

[1] E. F. Alves, L. Polleux, G. Guerassimoff et al., "Allocation of spinning reserves in autonomous grids considering frequency stability constraints and short-term solar power variations," *IEEE Access*, vol. 11, pp. 29896-29908, Mar. 2023.

[2] S. Zhong, X. Wang, B. Xu et al., "Hybrid network model based on data enhancement for short-term power prediction of new PV plants," *Journal of Modern Power Systems and Clean Energy*, vol. 12, no. 1, pp. 77-88, Jan. 2024.

[3] Y. Sun, Y. Zhou, S. Wang et al., "Nonparametric probabilistic prediction of regional PV outputs based on granule-based clustering and direct optimization programming," *Journal of Modern Power Systems and Clean Energy*, vol. 11, no. 5, pp. 1450-1461, Sept. 2023.

[4] V. R. da Rocha, R. S. Costa, F. R. Martins et al., "Variability index of solar resource based on data from surface and satellite," *Renewable Energy*, vol. 201, no. 1, pp. 354-378, Dec. 2022.

[5] I. K. Bazionis, M. A. Kousounadis-Knousen, P. S. Georgilakis et al., "A taxonomy of short-term solar power forecasting: classifications focused on climatic conditions and input data," *IET Renewable Power Generation*, vol. 17, no. 9, pp. 2411-2432, May 2023.

[6] L. Cheng, H. Zang, Z. Wei et al., "Short-term solar power prediction learning directly from satellite images with regions of interest," *IEEE Transactions on Sustainable Energy*, vol. 13, no. 1, pp. 629-639, Jan. 2022.

[7] J. Hurtt and K. Baker, "Sensitivity analysis of photovoltaic system design parameters to passively mitigate ramp rates," *IEEE Journal of Photovoltaics*, vol. 11, no. 2, pp. 545-551, Jan. 2021.

[8] H. A. H. Al-Hilfi, A. Abu-Siada, and F. Shahnia, "Estimating generated power of photovoltaic systems during cloudy days using gene expression programming," *IEEE Journal of Photovoltaics*, vol. 11 no. 1, pp. 185-194, Jan. 2021.

[9] F. P. M. Kreuwel, W. H. Knap, L. R. Visser et al., "Analysis of high frequency photovoltaic solar energy fluctuations," *Solar Energy*, vol. 206, pp. 381-389, Aug. 2020.

[10] R. P. Raj and A. Kowli, "Characterizing the ramps and noise in solar power imbalances," *Solar Energy*, vol. 247, pp. 531-542, Nov. 2022.

[11] H. Jain, M. Sengupta, A. Habte et al., "Quantifying solar PV variability at multiple timescales for power systems studies," in *Proceedings of IEEE Photovoltaic Specialists Conference*, Calgary, Canada, Jun. 2020, pp. 180-185.

[12] J. Marcos, L. Marroyo, E. Lorenzo et al., "Power output fluctuations in large scale PV plants: one year observations with one second resolution and a derived analytic model," *Progress in Photovoltaics: Research and Applications*, vol. 19, no. 2, pp. 218-227, Feb. 2011.

[13] M. Lave, R. J. Broderick, and M. J. Reno, "Solar variability zones: satellite-derived zones that represent high-frequency ground variability," *Solar Energy*, vol. 151, pp. 119-128, Jul. 2017.

[14] G. M. Lohmann, "Irradiance variability quantification and small-scale averaging in space and time: a short review," *Atmosphere*, vol. 9, no. 7, p. 264, Jul. 2018.

[15] S. Poddar, M. Kay, A. Prasad et al., "Changes in solar resource intermittency and reliability under Australia's future warmer climate," *Solar Energy*, vol. 266, p. 112039, Dec. 2023.

[16] D. Yang and J. M. Bright, "Worldwide validation of 8 satellite-derived and reanalysis solar radiation products: a preliminary evaluation and

overall metrics for hourly data over 27 years," *Solar Energy*, vol. 210, pp. 3-19, Nov. 2020.

[17] M. R. Aldeman, J. H. Jo, D. G. Loomis *et al*., "Reduction of solar photovoltaic system output variability with geographical aggregation," *Renewable and Sustainable Energy Transition*, vol. 3, p. 100052, Aug. 2023.

[18] B. E. Ellis, N. Pearre, and L. Swan, "Power ramp rates and variability of individual and aggregate photovoltaic systems using measured production data at the municipal scale," *Solar Energy*, vol. 220, pp. 363-370, May 2021.

[19] R. Kini, D. Raker, T. Stuart *et al*., "Mitigation of PV variability using adaptive moving average control," *IEEE Transactions on Sustainable Energy*, vol. 11, no. 4, pp. 2252-2262, Oct. 2020.

[20] K. Lappalainen, G. Wang, and J. Kleissl, "Estimation of the largest expected photovoltaic power ramp rates," *Applied Energy*, vol. 278, p. 115636, Nov. 2020.

[21] M. Talvi, T. Roinila, and K. Lappalainen, "Effects of ramp rate limit on sizing of energy storage systems for PV, wind and PV-wind power plants," *Energies*, vol. 16, no. 11, p. 4313, May 2023.

[22] Â. Frimane, T. Soubdhan, J. M. Bright *et al*., "Nonparametric Bayesian-based recognition of solar irradiance conditions: application to the generation of high temporal resolution synthetic solar irradiance data," *Solar Energy*, vol. 182, pp. 462-479, Apr. 2019.

[23] Y. Tang, J. Cheng, Q. Duan *et al*., "Evaluating the variability of photovoltaics: a new stochastic method to generate site-specific synthetic solar data and applications to system studies," *Renewable Energy*, vol. 133, pp. 1099-1107, Apr. 2019.

[24] W. Zhang, W. Kleiber, A. R. Florita *et al*., "A stochastic downscaling approach for generating high-frequency solar irradiance scenarios," *Solar Energy*, vol. 176, pp. 370-379, Dec. 2018.

[25] M. Lave, J. Kleissl, and J. S. Stein, "A wavelet-based variability model (WVM) for solar PV power plants," *IEEE Transactions on Sustainable Energy*, vol. 4, no. 2, pp. 501-509, Apr. 2013.

[26] A. R. Dyreson, E. R. Morgan, S. H. Monger *et al*., "Modeling solar irradiance smoothing for large PV power plants using a 45-sensor network and the wavelet variability model," *Solar Energy*, vol. 110, pp. 482-495, Oct. 2014.

[27] K. Lappalainen and S. Valkealahti, "Output power variation of different PV array configurations during irradiance transitions caused by moving clouds," *Applied Energy*, vol. 190, pp. 902-910, Mar. 2017.

[28] X. Chen, Y. Du, E. Lim *et al*., "Power ramp rates of utility-scale PV systems under passing clouds: module-level emulation with cloud shadow modeling," *Applied Energy*, vol. 268, p. 114980, Jun. 2020.

[29] H. G. Beyer, A. Hammer, J. Luther *et al*., "Analysis and synthesis of cloud pattern for radiation field studies," *Solar Energy*, vol. 52, no. 5, pp. 379-390, May 1994.

[30] C. Cai and D. C. Aliprantis, "Cumulus cloud shadow model for analysis of power systems with photovoltaics," *IEEE Transactions on Power Systems*, vol. 28, no. 4, pp. 4496-4506, Nov. 2013.

[31] R. Ahmad, A. F. Murtaza, H. A. Sher *et al*., "An analytical approach to study partial shading effects on PV array supported by literature," *Renewable & Sustainable Energy Reviews*, vol. 74, pp. 721-732, Jul. 2017.

[32] S. F. A. Shah, I. A. Khan, and A. H. A. Khan, "Performance evaluation of two similar 100 MW solar PV plants located in environmentally homogeneous conditions," *IEEE Access*, vol. 7, pp. 161697-161707, Nov. 2019.

[33] S. Kuszamaul, A. Ellis, J. Stein *et al*., "Lanai high-density irradiance sensor network for characterizing solar resource variability of MW-scale PV system," in *Proceedings of IEEE Photovoltaic Specialists Conference*, Honolulu, USA, Jun. 2010, pp. 283-288.

[34] W. Xiao, *Photovoltaic Power System: Modelling, Design and Control,* 1st ed., Hoboken: John Wiley & Sons Ltd., 2017.

[35] M. L. López, G. G. Palancar, and B. M. Toselli, "Effects of stratocumulus, cumulus, and cirrus clouds on the UV-B diffuse to global ratio: experimental and modeling results," *Journal of Quantitative Spectroscopy and Radiative Transfer*, vol. 113, no. 6, pp. 461-469, Apr. 2012.

[36] J. S. Stein, C. W. Hansen, and M. J. Reno, "The variability index: a new and novel metric for quantifying irradiance and PV output variability," in *Proceedings of World Renewable Energy Forum*, Denver, USA, May 2012, pp. 2764-2770.

[37] E. B. Dilger and R. V. de Oliveira, "Power reserve control for utility-scale PV power plants under cloud conditions," *Electric Power Systems Research*, vol. 229, p. 110099, Apr. 2024.

[38] A. Cabrera-Tobar, E. Bullich-Massagué, M. Aragüés-Peñalba *et al*., "Topologies for large scale photovoltaic power plants," *Renewable & Sustainable Energy Reviews*, vol. 59, pp. 309-319, Jun. 2016.

[39] V. D. Paduani, H. Yu, B. Xu *et al*., "A unified power-setpoint tracking algorithm for utility-scale PV systems with power reserves and fast frequency response capabilities," *IEEE Transactions on Sustainable Energy*, vol. 13, no. 1, pp. 479-490, Jan. 2022.

[40] M. Haghighat, M. Niroomand, H. D. Tafti *et al*., "A review of state-of-the-art flexible power point tracking algorithms in photovoltaic systems for grid support: classification and application," *Journal of Modern Power Systems and Clean Energy*, vol. 12, no. 1, pp. 1-21, Jan. 2024.

[41] L. Hassaine, E. Olias, J. Quintero *et al*., "Overview of power inverter topologies and control structures for grid connected photovoltaic systems," *Renewable & Sustainable Energy Reviews*, vol. 30, pp. 796-807, Feb. 2014.

[42] S. A. Julien, A. Sajadi, and B. M. Hodge, "Hierarchical control of utility-scale solar PV plants for mitigation of generation variability and ancillary service provision," *IEEE Transactions on Sustainable Energy*, vol. 13 no. 3, pp. 1383-1395, Jul. 2022.

[43] P. Kuhn, M. Wirtz, S. Wilbert *et al*., "Field validation and benchmarking of a cloud shadow speed sensor," *Solar Energy*, vol. 173, pp. 229-245, Mar. 2018.

[44] J. Martins, S. Spataru, D. Sera *et al*., "Comparative study of ramp rate control algorithms for PV with energy storage systems," *Energies*, vol. 12, no. 7, p. 1342, Apr. 2019.

[45] J. Marcos, L. Marroyo, E. Lorenzo *et al*., "From irradiance to output power fluctuations: the PV plant as a low pass filter," *Progress in Photovoltaics: Research and Applications*, vol. 19, pp. 505-510, Jan. 2011.

[46] G. M. Lohmann, "Irradiance variability quantification and small-scale averaging in space and time: a short review," *Atmosphere*, vol. 9, p. 264, Jul. 2018.

Eric Bernard Dilger received the B.S. and M.S. degrees in electrical engineering from Federal University of Technology, Paraná, Brazil, in 2019 and 2023, respectively. He is currently working as a Professor at the Federal Institute of Paraná, Paraná, Brazil. His research interests include power system dynamics and control, and design, operation, dynamics, and control of photovoltaic generation.

Ricardo Vasques de Oliveira received the B.S. degree in electrical engineering from the Federal University of Mato Grosso, Mato Grosso, Brazil, and the M.S. and Ph.D. degrees in electrical engineering from University of São Paulo (EESC/USP), São Paulo, Brazil, in 2001, 2003, and 2006, respectively. He has been Professor and Researcher at the Federal University of Technology, Paraná, Brazil, since 2007. His research interests include power system dynamics and control, design, operation, dynamics, and control of wind generation, photovoltaic generation, and microgrid, voltage and frequency control, and operation and control of distribution systems.